Draft version March 27, 2014
Preprint typeset using LaTeX style emulateapj v. 5/2/11

arXiv:1403.6743v1 [astro-ph.CO] 26 Mar 2014

SECONDARY MODELS FOR RADIO MINI-HALOS IN GALAXY CLUSTERS WITH MHD SIMULATIONS OF GAS SLOSHING

J.A. ZuHone[1], G. Brunetti[2], S. Giacintucci[3], M. Markevitch[1]

Draft version March 27, 2014

ABSTRACT

We present simulations of a radio minihalo in a galaxy cluster core with sloshing cold fronts, under the assumption that the source of the synchrotron-emitting electrons is hadronic interactions between cosmic-ray protons with the thermal intracluster gas. This is an alternative to the hypothesis where the cosmic ray electrons are reaccelerated by the intracluster turbulence, which we have discussed in an earlier work. We follow the evolution of cosmic-ray electron spectra associated with passive tracer particles, taking into account the time-dependent injection of new electrons from the hadronic interactions and energy losses along each particle's trajectory. We then simulate the radio emission from these particles. The drop in radio emission at the cold front surfaces is less prominent than that in our previous simulations, based on electron reacceleration from sloshing-induced turbulence, where the emission is definitively confined to the regions within cold fronts. The result is that the emission is overall more spatially extended than found in some observed minihalos. We also explore spectral effects induced by the change of physical conditions in the ICM. Rapid changes in magnetic field strength are expected to produce radio spectra steeper than those calculated assuming stationary conditions, but we find this effect is marginal, with differences in the synchrotron spectral index $\Delta\alpha \lesssim 0.15$ between $\nu \sim$ 300-1400 MHz and $\Delta\alpha \lesssim 0.25$ between $\nu \sim$ 60-153 MHz.

1. INTRODUCTION

A number of relaxed, cool-core clusters are hosts to faint, diffuse synchrotron radio sources called "radio minihalos", with a radius comparable to the size of the cooling region ($r \lesssim$ 100-300 kpc) and a steep spectrum ($\alpha \gtrsim 1$; $S_\nu \propto \nu^{-\alpha}$). They arise from cosmic-ray electrons (hereafter CRe) emitting in the $\sim \mu$G magnetic fields in the cluster. These are relatively rare sources, with currently only around 10 clusters with confirmed detections. Examples include Perseus (Burns et al. 1992), A2029 (Govoni et al. 2009), Ophiuchus (Govoni et al. 2009; Murgia et al. 2010), RXC J1504.1-0248 (Giacintucci et al. 2011), and RXJ 1347-1145 (Gitti et al. 2007), along with the newest detections in Giacintucci et al. (2014a). The origin of radio mini-halos in cool core clusters, as well as their possible connection with giant radio halos, is still unclear (see, e.g. Brunetti & Jones 2014, for a review). Though the clusters which host these sources typically also have active galactic nuclei, due to the fact that the radiative timescale of the electrons at the required energies for the observed emission ($\sim 10^8$ years) is much shorter than the time required for these electrons to diffuse across the cooling region, they alone cannot account for the origin of minihalos.

Most cool-core clusters also possess spiral-shaped cold fronts (Ghizzardi et al. 2010), which are believed to be the product of the central cold gas "sloshing" in the cluster potential minimum due to interactions with subclusters. A number of simulation works have investigated the importance of this phenomenon (e.g. Ascasibar & Markevitch 2006; ZuHone et al. 2010; Roediger et al. 2011). Most relevant for this work, in ZuHone et al. (2011, hereafter ZML11) we showed that such magnetic field amplification occurs near the cold front surfaces due to the local velocity shear. Mazzotta & Giacintucci (2008) first discovered a correlation between sloshing cold fronts and minihalo emission in two galaxy clusters, and a few other examples have since been observed (e.g. Hlavacek-Larrondo et al. 2013; Giacintucci et al. 2014a), suggesting a causal connection between sloshing motions and radio minihalos.

One possible origin for the CRe which produce the observed synchrotron radiation of minihalos is reacceleration of a lower energy population of CRe due to turbulence (Gitti et al. 2002). In a previous work (ZuHone et al. 2013, hereafter Z13), we simulated relativistic particle reacceleration due to MHD turbulence in a sloshing cluster core. The sloshing motions produced turbulent velocities of $\delta v \sim 100 - 200$ km s^{-1} on scales of 10s of kpc within the sloshing region. We showed that radio emission consistent with the properties of observed minihalos could be produced by assuming an initial population of CRe with $\gamma \sim 100 - 500$ spread throughout the cluster core, which were then accelerated by the turbulence initiated by the sloshing.

There is an alternative perspective on the origin diffuse radio emission in clusters of galaxies, known as the "hadronic" or "secondary" model (see, e.g. Pfrommer & Enßlin 2004; Keshet & Loeb 2010; Fujita & Ohira 2012). Cosmic-ray protons (hereafter CRp) are believed to fill the cluster volume, having been accelerated from the thermal population to relativistic energies by supernovae, AGN, and shocks associated with cosmological structure formation (for a review see Brunetti & Jones 2014) These protons will undergo interactions with the thermal proton population, produc-

[1] Astrophysics Science Division, Laboratory for High Energy Astrophysics, Code 662, NASA/Goddard Space Flight Center, Greenbelt, MD 20771, USA
[2] INAF Istituto di Radioastronomia, via Gobetti 101, 40129 Bologna, Italy
[3] Department of Astronomy, University of Maryland, College Park, MD, 20742-2421, USA

ing pions which will decay into secondary products, including cosmic-ray electrons and positions:

$$p_{\rm th} + p_{\rm CR} \rightarrow \pi^0 + \pi^+ + \pi^- \quad (1)$$
$$\pi^\pm \rightarrow \mu^\pm + \nu_\mu/\bar{\nu}_\mu \rightarrow e^\pm + \nu_e/\bar{\nu}_e + \nu_\mu + \bar{\nu}_\mu$$
$$\pi^0 \rightarrow 2\gamma$$

Since the CRp have very long radiative loss times compared with the age of the cluster, these interactions should continuously provide a fresh population of CRe at a range of energies. In this model, it is these CRe that produce the observed radio emission. These hadronic interactions should also produce a flux of γ-rays, but so far no confirmed detections of such emission from galaxy clusters have been made. Upper limits on the γ-ray flux from several experiments (see, e.g. MAGIC Collaboration et al. 2011; The *Fermi*-LAT Collaboration et al. 2013; Prokhorov & Churazov 2013) indicate the ratio of the CRp energy to the thermal energy of the gas is at most ∼1-2%. Still, contrary to the case of nearby giant radio halos, these limits do not put significant tension on a secondary origin of mini-halos (Brunetti & Jones 2014). For example, Zandanel et al. (2014) proposed that mini-halos are primarily of hadronic origin, while giant radio halos experience a transition from a central hadronic emission to a leptonic emission component in the external regions due to CRe reacceleration.

The spectrum of CRp is expected to be roughly a power-law in the relevant energy range of $E_p \sim$ a few to 100 GeV with spectral index $\alpha_p \sim 2-3$. In this model, under relatively quiescent conditions, the electron spectrum will reach a steady-state condition where the energy losses and the gains due to injection balance each other out (Sarazin 1999). At high energies, where the radiative (synchrotron and inverse-Compton) losses dominate, the CRe spectrum has the form $N(E) \propto E^{-\alpha_e}$, which results in a synchrotron emissivity that depends on the properties of the CRp and the plasma as

$$j_\nu \propto n_{\rm th} \epsilon_{\rm CRp} \frac{B^{1+\alpha}}{B^2 + B_{\rm CMB}^2} \nu^{-\alpha} \quad (2)$$

where $n_{\rm th}$ is the number density of thermal particles, B is the magnetic field strength, $B_{\rm CMB} \approx 3.25(1+z)^2$ μG is the equivalent magnetic field strength of the CMB, α is the synchrotron spectral index, and $\epsilon_{\rm CRp}$ is the energy density of CRp. Under the steady-state assumption and where radiative losses dominate, $\alpha = \alpha_p/2 \sim 1$. This implies that for $B \gg B_{\rm CMB}$ the radio emission is roughly independent of the magnetic field strength and for $B \ll B_{\rm CMB}$ it is suppressed. Keshet & Loeb (2010) suggested that due to the magnetic field amplification underneath the cold fronts that the radio emission would sharply drop at the cold front surface as B becomes less than $B_{\rm CMB}$.

Though this spectral index value is at the consistent with the range of spectral indices found in minihalo sources, this simplified picture implies that the synchrotron spectrum should have the same slope everywhere throughout the minihalo. So far, the few available spatially-resolved observations of the minihalo spectral slopes indicate that this is likely not the case (Sijbring 1993; Murgia et al. 2010; Gitti 2013; Giacintucci et al. 2014b), although more detailed analyses are needed. Another prediction, distinct from the turbulent acceleration model, is that this power-law slope should extend to high frequencies, without any steepening. One way of achieving a spatially and energetically varying spectral index is to assume that some locations in the core deviate from a steady-state condition. In particular, Keshet (2010) demonstrated a rapidly increasing magnetic field strength will result in a steeper spectrum than the steady-state case (so long as $B \gg B_{\rm CMB}$). Magnetic field amplification near cold front surfaces could possibly cause spectral steepening of the radio emission moving outward along the spiral arm of the sloshing cold fronts, away from the cluster center.

In this work, we use the same cluster setup as in Z13 to determine the predictions of the hadronic/secondary model for the production of minihalos. We follow the evolution of CRe spectra associated with passive tracer particles which are advected with the flow of gas, determining the injection into and radiative losses on the spectrum along each trajectory. In this way we can determine how deviations from a steady-state configuration affect the surface brightness of the minihalo emission as well as its spectral shape.

This paper is organized as follows. In Section 2 we describe our method for evolving the CRe spectra and our assumptions regarding their injection by hadronic processes. In Section 3 we detail the results of our simulations. In Section 4 we discuss the implications of this work, and in Section 5 we make our conclusions. Throughout this work we assume a flat ΛCDM cosmology with $h = 0.7$ and $\Omega_{\rm m} = 0.3$.

2. METHOD

We performed our MHD simulation of gas sloshing using the FLASH code (Dubey et al. 2009). The details of this simulation, including of the passive tracer particles which serve as the sites for the injection and evolution of relativistic electrons, are given in Z13, and we refer the reader to Section 2.1 of that work. For completeness, we note that our setup consists of a large, cool-core cluster with $M \sim 10^{15}$ $M_\odot$, $T_X \sim 7$ keV, and a magnetic field profile with a central value of $B_0 \sim 10$ μG and that declines with radius as the square root of the thermal pressure (e.g., a constant $\beta = p_{\rm th}/p_B$). Gas sloshing is initiated in this cluster by an encounter with a small gasless subcluster.

2.1. *Method for Evolution of the Relativistic Electron Spectrum*

In this work, CRe reacceleration due to turbulence and/or shocks is neglected. To evolve the time-dependent spectrum $N(p,t)$ of the CRe momentum p along the tracer particle trajectories, we employ a kinetic equation:

$$\frac{\partial N(p,t)}{\partial t} + \frac{\partial}{\partial p}\left[N(p,t)\frac{dp}{dt}\right] = Q(p,t) \quad (3)$$

where dp/dt is the sum of the standard radiative and Coulomb losses:

$$\frac{dp}{dt} = \left.\frac{dp}{dt}\right|_{\rm rad} + \left.\frac{dp}{dt}\right|_{\rm coul} \quad (4)$$

$$\left.\frac{dp}{dt}\right|_{\rm rad} = -4.8\times10^{-4} p^2 \left[\left(\frac{B_{\mu\rm G}}{3.25}\right)^2 + (1+z)^4\right] \quad (5)$$

$$\left.\frac{dp}{dt}\right|_{\rm coul} = -3.3\times10^{-29} n_{\rm th}\left[1+\ln\left(\frac{\gamma/n_{\rm th}}{75}\right)\right], \quad (6)$$

where the redshift is evolved according to our assumed cosmology. We assign $z = 0$ to the epoch $t = 5$ Gyr of the simulation, in order to reproduce some of the observed nearby clusters exhibiting cold fronts in their cores.

To solve this kinetic equation we logarithmically sampled the CRe spectrum $N(p)$ 100 times in the range of $p/m_e c \in [10, 10^5]$, and evolved it on this momentum grid forward in time using a finite difference method. At each timestep, we separate the calculation into two steps, "advection" and "source term", using operator splitting. In the "advection" step, we compute the change in the spectrum in each momentum cell due to the change in the flux of electrons $\partial/\partial p[N dp/dt]$ from the adjacent cells on the momentum grid. To ensure stability, we applied a minmod slope limiter to this flux at each cell boundary. Following the "advection" step, we apply the "source term" operation $Q(p,t)$ by computing the change in the spectrum at each momentum cell using the time-interpolated value of the source term.

Finally, at the lower momentum boundary we impose outflow boundary conditions, and at the higher momentum boundary we extend the spectrum into the boundary cells with a constant logarithmic slope, a sensible choice since at such high energies in a steady-state the spectrum is dominated by the competition between injection and radiative losses and the spectrum is essentially a pure power law with index $\alpha_p + 1$.

As in Z13, the simulations of the evolution of the electron spectra are performed in post-processing on the passive tracer particles from the MHD simulation. These particles consist of datasets that are spaced apart in time by 10 Myr. The local conditions of the gas at any time, such as the density of thermal particles and the magnetic field, are determined by linearly interpolating between their values at the epochs corresponding to the datasets.

2.2. *Modeling the Injection of Secondary Electrons*

The injection rate is determined by the rate of interactions of CRp with the thermal population. We assume that the CRp momentum ($p_p = \gamma_p \beta_p m_p c$) spectrum can be approximated by a single power-law, $N_p(p_p) = C_p p_p^{-\alpha_p}$, where C_p is a normalization constant and $\alpha_p = 2.3$, a value within the range ($\approx$ 2.0-2.5) implied by various mechanisms capable of injecting relativistic CRp into the ICM (e.g., structure formation shocks, injection by radio galaxies, supernova remnants; Pfrommer & Enßlin 2004; Keshet & Loeb 2010).

For consistency with previous literature, we follow in part the derivation of the electron source function of Pfrommer et al. (2008).[4] The pion production spectrum is

$$s_\pi(p_\pi, p_p) = c n_{\rm th}\xi(p_p)\sigma^\pi_{\rm pp}(p_p)\delta_D(p_\pi - \langle p_\pi\rangle) \quad (7)$$

where $\sigma^\pi_{\rm pp}$ is the inelastic p-p cross section and $\langle p_\pi\rangle$ is the average momentum of a single produced pion, and we have employed the delta-function approximation. We may integrate this source function with respect to the CRp momentum distribution to obtain

$$s_{\pi^\pm}(p_\pi) = \frac{2}{3} q_\pi(p_\pi) = \frac{2}{3}\int_{-\infty}^{\infty} f(p_p) s_\pi(p_\pi, p_p) dp_p \quad (8)$$

where $\langle p^\pm_\pi\rangle = p_p/4$.

Using the transformation law for distribution functions and using the mean value of the CRe momentum in the relativistic limit, we approximate the CRe momentum source function by

$$Q(p)dp = s^\pm_\pi(p_\pi)\frac{dp_\pi}{dp}dp \quad (9)$$

$$= \frac{4}{3} 16^{1-\alpha_p} c n_{\rm th} C_p \sigma_{\rm pp}(16p) p^{-\alpha_p} dp \quad (10)$$

assuming that the mean momentum of the produced secondary electrons in the laboratory frame is given by $\langle p_e\rangle = \frac{1}{4}\langle p^\pm_\pi\rangle$. Previous works (see, e.g. Dolag & Enßlin 2000; Pfrommer & Enßlin 2004; Pfrommer et al. 2008) have commonly approximated the proton-proton cross section by an energy-averaged constant value, which results in a pure power-law form for the source function, and hence the steady-state electron CRe is also a power-law with spectral index $\alpha_e = \alpha_p + 1$, and the synchrotron spectral index is $\alpha = (\alpha_e - 1)/2 = \alpha_p/2$. In this work we also account for the weak energy dependence of the cross section on the proton energy found by Kelner et al. (2006):

$$\sigma_{\rm pp}(E_p) = (34.3 + 1.88L + 0.25L^2)\times\left[1 - \left(\frac{E_{\rm th}}{E_p}\right)\right]^2 \rm mb \quad (11)$$

where $L = \ln(E_p/1\ \rm TeV)$ and $E_{\rm th} = m_p + 2m_\pi + m_\pi^2/2m_p = 1.22\times10^{-3}$ TeV is the threshold energy of production of π^0 mesons.

Our inclusion of a weak energy dependence of $\sigma_{\rm pp}$ results in a steady-state CRe spectrum with a slope that is slightly shallower than $\alpha_p + 1$. From numerical tests assuming a steady-state spectrum of CRe we have determined that the observed spectral index for magnetic fields of $B \sim 0.1-10\ \mu$G will be roughly within the range of $\alpha \sim 1.09 - 1.17$, with a typical value of $\alpha \approx 1.13$ (see Figure 3),[5] a very minor deviation from the value of 1.15 expected by treating $\sigma_{\rm pp}$ as constant.

2.3. *Modeling the Cosmic-Ray Protons*

The propagation of CRs in the ICM is determined by a combination of diffusion (including turbulent transport) and convection (see Brunetti & Jones 2014, for a review). In our simulations, diffusion and turbulent transport of the CRp are neglected. In general, diffusion (along the field lines) is an energy-dependent process that depends

[4] Note that in our derivation the symbol p corresponds to the particle momentum but in their derivation it corresponds to the momentum nomalized by mc.

[5] Unless otherwise noted we fit for α between 327 and 1420 MHz.

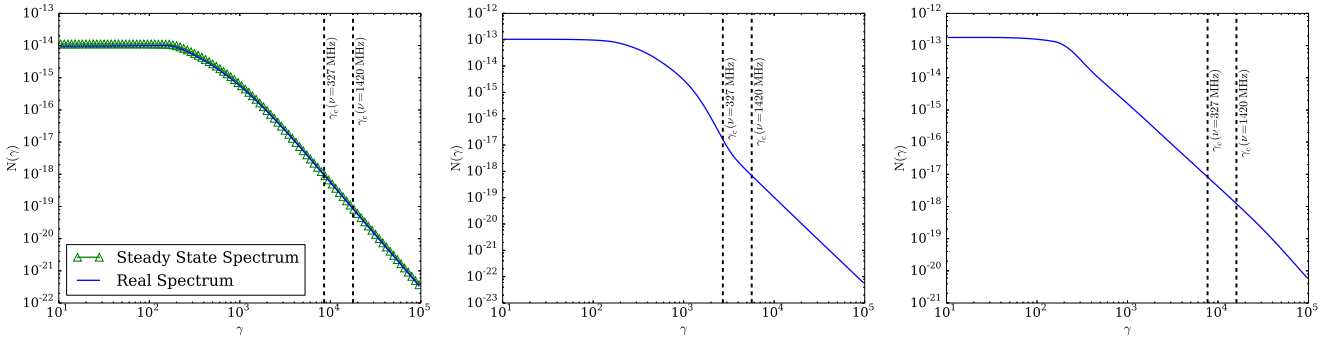

FIG. 1.— CRe spectra under various conditions. Left: A typical CRe spectrum for a particle close to the steady-state condition. The blue line indicates the real particle spectrum,and the green line indicates the steady-state spectrum for the same conditions. Center: A typical CRe spectrum for a particle with a steep synchrotron spectrum. Right: A typical CRe spectrum for a particle with a shallow synchrotron spectrum. In each panel, the vertical dashed lines indicate the characteristic CRe energies corresponding to the frequencies of 327 and 1420 MHz.

on the spectrum of MHD waves and on the physics of the interplay/scatter between CRs and these waves. The time necessary for CRs to diffuse over distances L is $\tau_{\rm diff} \sim 1/4L^2/D$, where D is the spatial diffusion coefficient. This process is expected to affect our results if CRs diffuse on scales of about 100 kpc within a time frame of ~ 1 Gyr, which would imply a diffusion coefficient $D \geq 10^{30}{\rm cm}^2/{\rm s}$ that is very large, although it cannot be ruled out.

At the same time, CRs are expected to be transported as passive scalars by the turbulent gas-flow (Brunetti & Jones 2014). On scales similar to that of the turbulence or larger, this induces a diffusive process that is energy independent with a diffusion coefficient $D \sim V_o l_o$, where V_o and l_o are the velocities and scales of the largest turbulent eddies. According to numerical simulations of sloshing motions in galaxy clusters, $D < 10^{29}$ cm^2/s (Vazza et al. 2012), implying typical transport-diffusion scales of $\sim 10-50$ kpc on a timescale of 1 Gyr for CRp.

Since we do not model these processes explicitly in our simulation, we have chosen to model the evolution of the CRe spectrum under the assumption of a peaked CRp profile with $\epsilon_{\rm CRp} = X_{\rm CRp}\epsilon_{\rm th}$. We choose a reference value of $X_{\rm CRp} = 0.02$, at the upper limit placed on the energy density of cosmic-ray protons by the Fermi, HESS, and MAGIC non-detections of γ-ray emission from neutral pions, which are produced in the same hadronic interactions and subsequently decay (Ackermann et al. 2010; MAGIC Collaboration et al. 2011; The *Fermi*-LAT Collaboration et al. 2013; Prokhorov & Churazov 2013).

3. RESULTS

3.1. *Tracer Particles Evolution*

To get a sense for how deviations from steady-state conditions affect the resulting electron spectrum of the particles, we will first examine the properties of the tracer particles.

The left panel of Figure 1 shows a typical example of a tracer particle with a steady-state CRe spectrum at the epoch $t = 3.5$ Gyr, approximately 2 Gyr past the core passage, a moment at which there is strong magnetic field amplification due to sloshing. The magnetic field strength for this particular particle, however, is not changing rapidly at this epoch. The black dashed lines indicate the values of γ that roughly correspond to the frequencies of 327 MHz and 1420 MHz at $B \approx 1$ μG. At low energies, where no injection occurs (due to the energy threshold for pion production, cf. Equation 11) and Coulomb losses dominate, the spectrum is relatively flat, whereas at higher energies it transitions to a power-law shape with $\alpha_e \approx 1.13$, where it is dominated by the tradeoff between injection and radiative losses. For comparison, the steady-state spectrum for the same gas and magnetic field conditions is also plotted in the left panel of Figure 1. The near equivalence of these two spectra indicates that the magnetic field strength and local density of particles are varying smoothly enough that the steady-state assumption is adequate.

The center panel of Figure 1 shows a typical example of a CRe spectrum of a tracer particle with a steep spectrum ($\alpha \approx 2$) at the epoch $t = 3.5$ Gyr. The magnetic field of this particle is undergoing significant amplification at this epoch. The black dashed lines indicate the values of γ that roughly correspond to the frequencies of 327 MHz and 1420 MHz at $B \approx 12$ μG. This spectrum, in contrast to the example spectrum that is close to the steady-state case, has a steep transition segment between the flat segment and the high-energy, $\alpha \approx 1.13$ segment which is determined by the tradeoff between injection and radiative losses.

The right panel of Figure 1 shows a typical example of a CRe spectrum of a tracer particle with a shallow spectrum ($\alpha \approx 0.8$) at the epoch $t = 3.5$ Gyr. The magnetic field strength of this particle is decreasing rapidly at this epoch. The black dashed lines indicate the values of γ that roughly correspond to the frequencies of 327 MHz and 1420 MHz at $B \approx 2.3$ μG. Over most of the range of particle energies, the spectral index is nearly constant, except at very high energies where it steepens due to the $\propto p^2$ dependence of the radiative losses.

It is instructive to examine the behavior of the spectral index of individual tracer particles to see how they change with time, and how this is related to the change with time of the magnetic field strength. Figure 2 shows the change in the spectral index and the magnetic field strength for three different particles each which at some point have steep and shallow spectra, respectively. The particles we have examined in Figure 1 are indicated by the green curves. These curves demonstrate that while most of the time the spectral index is fairly constant and

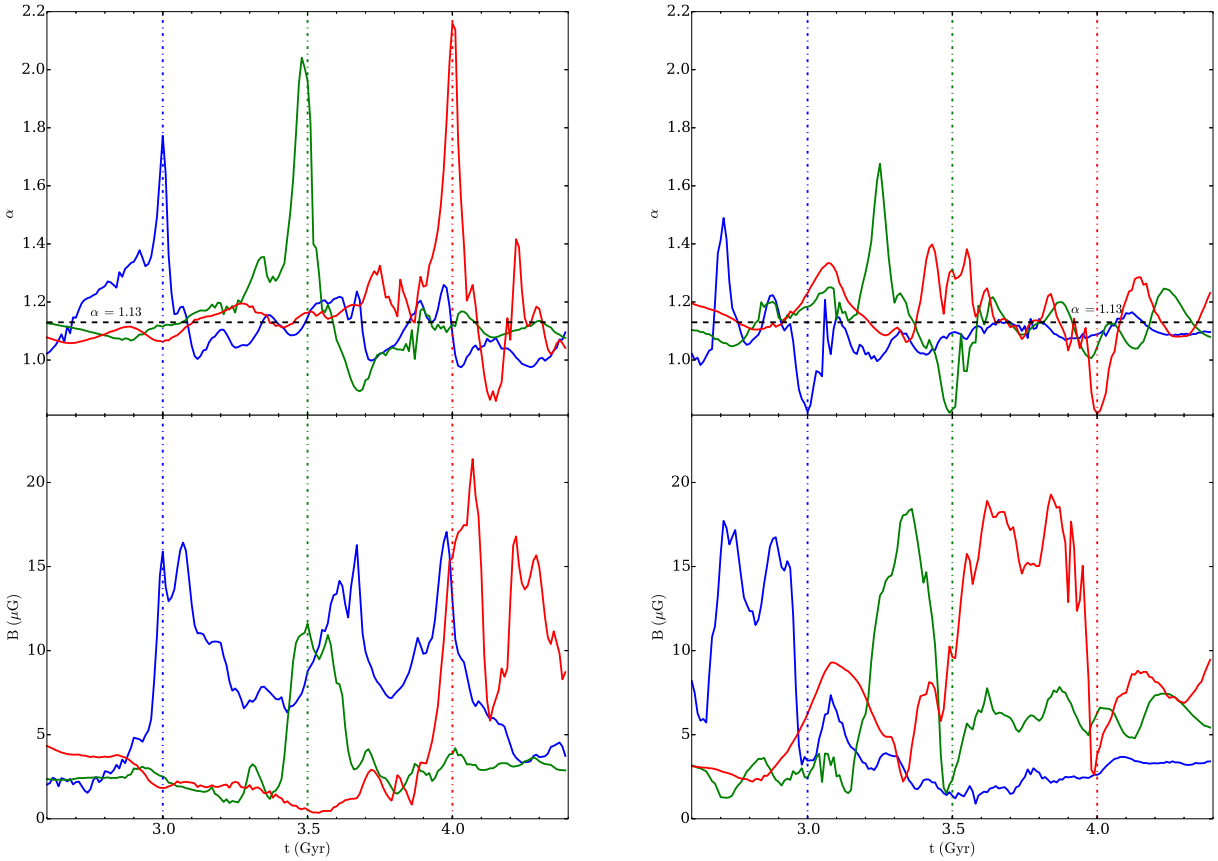

FIG. 2.— The evolution of the spectral index α and the magnetic field strength over time for selected particles. Left panel: Particles with steep spectra at a given epoch. Right panel: Particles with shallow spectra at a given epoch. Colored vertical dot-dashed lines indicate the epochs at which the extreme spectra occur for each particle. The horizontal black line indicates the approximate steady-state spectral index.

close to the steady-state value, that when the magnetic field increases rapidly it steepens, and when there is a rapid decrease it shallows. Although these effects are clear and theoretically expected (Keshet 2010) for particular tracers, we will show later (within this section and Section 3.3) that they cannot be representative.

Figure 3 shows a binned histogram of the radio spectral index α for all of the tracer particles at the epoch t = 3.5 Gyr. It has a narrow peak at $\alpha \approx 1.13$ and a small skew toward steeper spectral indices. The spectra of particles gets as flat as $\alpha \approx 0.8$ and as steep as $\alpha \sim 2$, but the number of these particles is dwarfed by the number of particles with spectra near the steady-state slope.

To get a sense of how the spectral index depends on the magnetic field, Figure 4 shows a phase plot of the radio spectral index versus the magnetic field strength for all of the particles in the simulation at the epoch $t = 3.5$ Gyr. At low magnetic field strengths, the fitted spectral index is very close to the steady-state expectation for nearly all tracer particles. The lack of steep spectral indices at these magnetic field strengths is readily understood; in this regime $B \ll B_{\rm CMB}$. The fact that we also do not observe many particles to have shallower spectra at these magnetic field strengths is due to the fact that at lower magnetic field strengths the observed synchrotron frequencies are sampling higher CRe energies, which will be within the part of the spectrum that is determined essentially completely by the tradeoff between radiative losses and injection.

As we go to higher magnetic field strengths, we see a broader distribution of spectral indices. Some of these spectra are somewhat flatter than the steady-state expectation, which correspond to particles where the magnetic field has been dropping rapidly (Figure 2). We find that the number of these particles increases up to $B \approx B_{\rm CMB}$ and then drops off, due to the increasing importance of the synchrotron over the inverse-Compton losses. Similarly, beginning around $B \approx B_{\rm CMB}$, the population of tracer particles with very steep spectra increases, corresponding to particles which are experiencing rapid increases in magnetic field strength. Nevertheless, the number of tracer particles with nearly steady-state spectra are dominant.

3.2. *Radio Intensity Maps*

Figure 5 shows maps of the X-ray emission of the thermal gas with contours of radio surface brightness at the frequency of 327 MHz overlaid for several different epochs of the simulation where the CRp energy follows the thermal energy density. The radio emission is fairly extended, and largely reflects the shape of the X-ray emission, which is expected in this case since $j_\nu \propto n_{\rm th}^2$, which is the same dependence on density as the X-ray emission. In particular, the spiral shape of the sloshing gas is readily seen in the radio contours.

Figure 6 shows profiles of the radio surface brightness

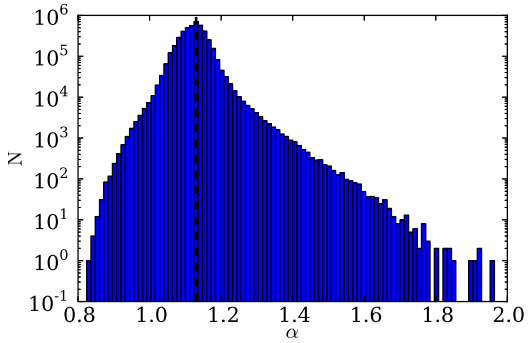

FIG. 3.— Binned histogram of tracer particle spectral indices at $t = 3.5$ Gyr. The dashed line indicates $\alpha = 1.13$.

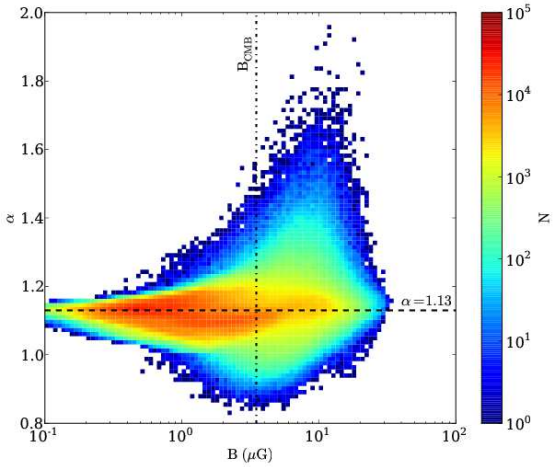

FIG. 4.— Phase plot of the synchrotron spectral index versus the magnetic field strength at the epoch $t = 3.5$ Gyr. The horizontal dashed line indicates $\alpha = 1.13$. The vertical dot-dashed line indicates where $B = B_{\rm CMB}$.

at the frequencies of 153, 327, and 1420 MHz corresponding to the black profiles in Figure 5 at the epoch $t = 3.5$ Gyr. Additionally, we have plotted the X-ray surface brightness along these profiles, and rescaled the overall normalization of both so that their radial dependence may be closely compared. Along the southern profiles, there are drops in radio emission across the cold front surface of an order of magnitude over ∼20 kpc. Along the NW profile, there is a similar drop, but it is over a larger radial range, ∼40 kpc. Along the NE profile, the radio emission drops off with radius at roughly the same rate as the X-ray emission. This plot also demonstrates that the overall shape of the radio emission is roughly independent of frequency along these profiles. This is expected, since once non-stationary effects play a minor role, the spectrum is a power law and the properties of the minihalo simply scale with frequency.

Some observed minihalos (e.g., RXJ 1720.1+26, MS 1455.0+2232 Mazzotta & Giacintucci 2008; Giacintucci et al. 2014b) typically have well-defined edges or appear to be confined to the core region, whereas others are more amorphous and/or extended (e.g., A2029, Ophiuchus Govoni et al. 2009; Murgia et al. 2010). In our reacceleration simulation of Z13, the radio emission was confined completely within the cold fronts, whereas the radio emission in our hadronic model is more extensive, particularly in the northern direction. To illustrate this, Figure 7 shows profiles of the radio emission along the northwest and southeast profiles from the hadronic simulation and the reacceleration simulation of Z13. Also plotted for comparison are 617 MHz radial profiles of the radio emission of RXJ 1720.1+26 (Giacintucci et al. 2014b), a galaxy cluster with sloshing cold fronts and a minihalo qualitatively similar in shape to that from our simulations. The radii of the profiles from RXJ 1720.1+26 have been rescaled such that the radii of the X-ray cold fronts are the same as in the simulations. Both the hadronic and reacceleration models result in drops in radio emission at the cold front profiles, but the drops in the reacceleration model are much steeper, and appear very similar to the drops in radio emission in RXJ 1720.1+26. There is a strong increase in the reacceleration profile at $r \sim 130$ kpc due to a patch of strong turbulence in this region, but even without this feature the drop in radio emission would be very pronounced. These results indicate that the behavior of the radial profile of the radio emission in minihalo sources at X-ray cold fronts are a test to constrain the origin scenario for these sources with future observations.

3.3. *Spectral Index*

Figure 8 shows the total radio spectrum in W/Hz within a radius of 300 kpc from the cluster potential minimum at several different epochs. Spectra from Z13 at similar epochs for the reacceleration model are also plotted for comparison. Our hadronic spectra are essentially power-law in shape over a large range of radio frequency, with the spectral index near the steady-state value $\alpha \approx 1.13$. In contrast, the reacceleration spectra gently steepen at high frequency, with different slopes depending on the epoch.

To create maps of the spectral index α, we reblock our intensity images by a factor of 8 and fit the spectrum in each reblocked pixel within a frequency range to a power-law, assuming 10% errors on the radio intensity in each band (typical errors for the radio intensity in minihalo observations are within the ∼5-10% range Giacintucci et al. 2014a,b). Figure 9 shows maps of the spectral index fitted between 327 and 1420 MHz at several epochs of the simulation. We find a fairly uniform spectral index throughout the sloshing region, close to the steady-state expectation of $\alpha \approx 1.13$, with the slopes in a narrow range of $\alpha \approx 1.0 - 1.3$. Near the cluster center, the spectrum becomes slightly flatter than the steady-state expectation ($\alpha \approx 1$), consistent with the increasing importance of Coulomb losses in the higher density region. Near the cold front edges, where the magnetic field is increasing rapidly due to shear amplification, we find that the spectral index increases to a maximum of $\alpha \approx 1.3$. Though we found that the spectral index for individual tracer particles in these highly magnetized regions could be as steep as $\alpha \approx 2$ (see Section 3.1), there are simply too few of these steep-spectrum particles to affect the spectrum of the emission projected along the line of sight. These results are inconsistent with the argument of Keshet (2010) for minihalos, who argued that rapid increases in magnetic field strength could explain steep-spectrum radio emission.

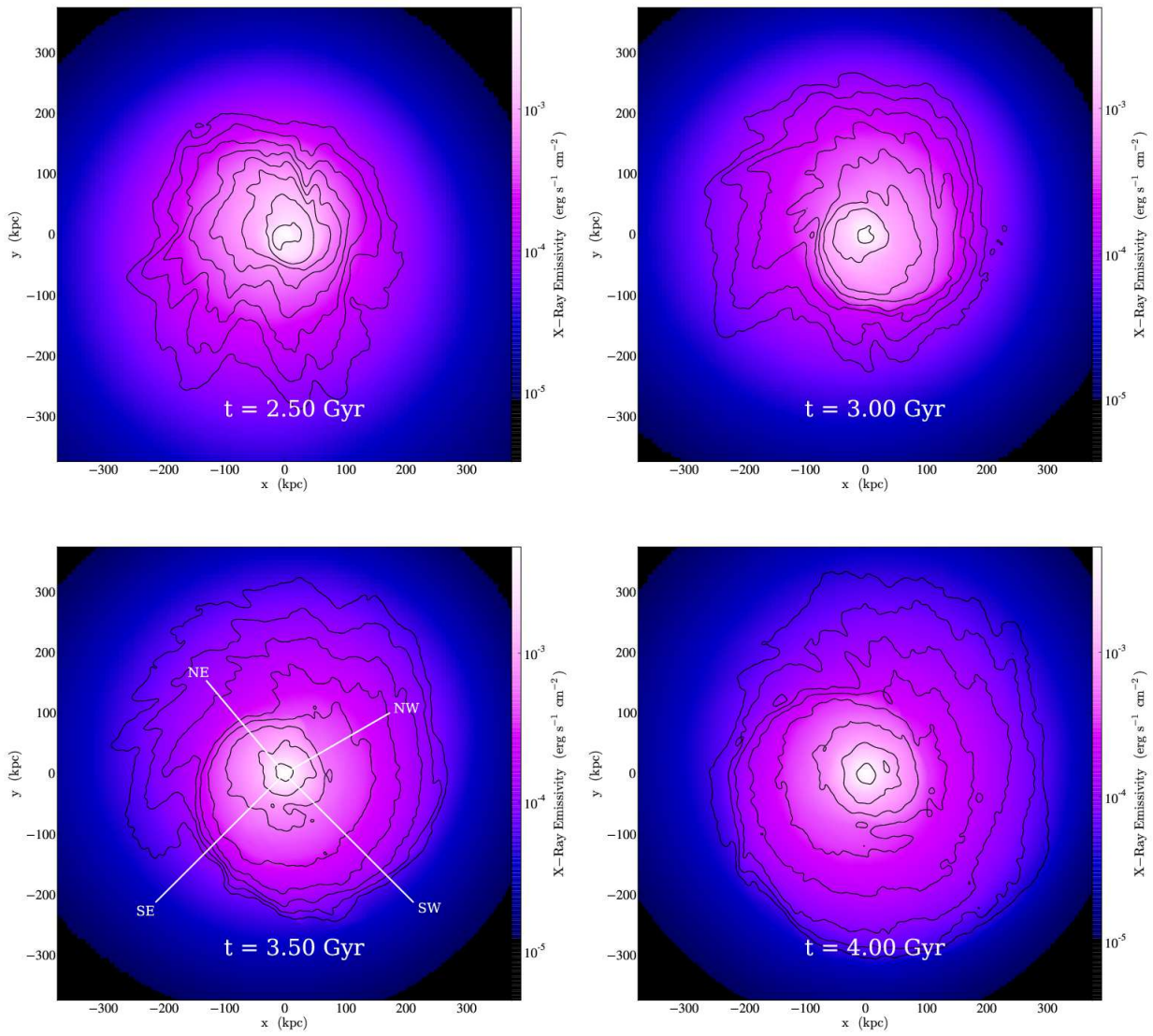

FIG. 5.— Projected maps of X-ray emission with 327 MHz radio contours overlaid at four different epochs of the simulation. Contours begin at 10^{-4} mJy arcsec^{-2} and increase by a factor of 2. Each panel is 750 kpc on a side. Profiles in the bottom-left panel correspond to those in Figure 6.

LOFAR[6] and LWA[7] will observe radio sources at much lower frequencies, down to ∼40 MHz. At these frequencies, the radiative loss timescales for the corresponding electrons are much longer and the effects of a change in the magnetic field would be more long-lasting. Figure 10 shows maps of the spectral index fitted between 60 and 153 MHz at the same epochs of the simulation. Here, there is again steepening of the radio spectrum at the cold front surface, but this too is limited, up to $\alpha \approx 1.4$, only slightly stronger than α measured in the higher-frequency band. At early epochs ($t \sim 2.5$ Gyr), we also see some marginal steepening of the radio spectrum just outside the core region (∼ 200 kpc), where the magnetic field has been recently strongly amplified due to the recent passage of the subcluster and resulting compression of the plasma.

[6] http://www.lofar.org
[7] http://www.phys.unm.edu/~lwa/index.html

4. DISCUSSION

4.1. *The Radial Extent of Minihalos*

In some observed minihalos, the radio emission is strongly confined to the core region, or the envelope of the cold fronts, if they are clearly observed. In our simulations, we find that the radial profile of the minihalo emission typically decreases at a more rapid rate approaching the cold fronts, but this is not always the case (in particular the NW profile from Figure 6).

A drop in radio emission across a cold front in the secondary model primarily results from two effects: the first is the density jump across the cold front, which is typically a factor of ∼1.5-2 for most cold fronts. The contribution of the density jump to the radio drop will be modest, since for the case where the CRp energy density is proportional to the thermal density, $j_\nu \propto n_{\rm th} P_{\rm th}$, and the thermal pressure is roughly continuous across cold front surfaces (except in a very thin layer at the cold

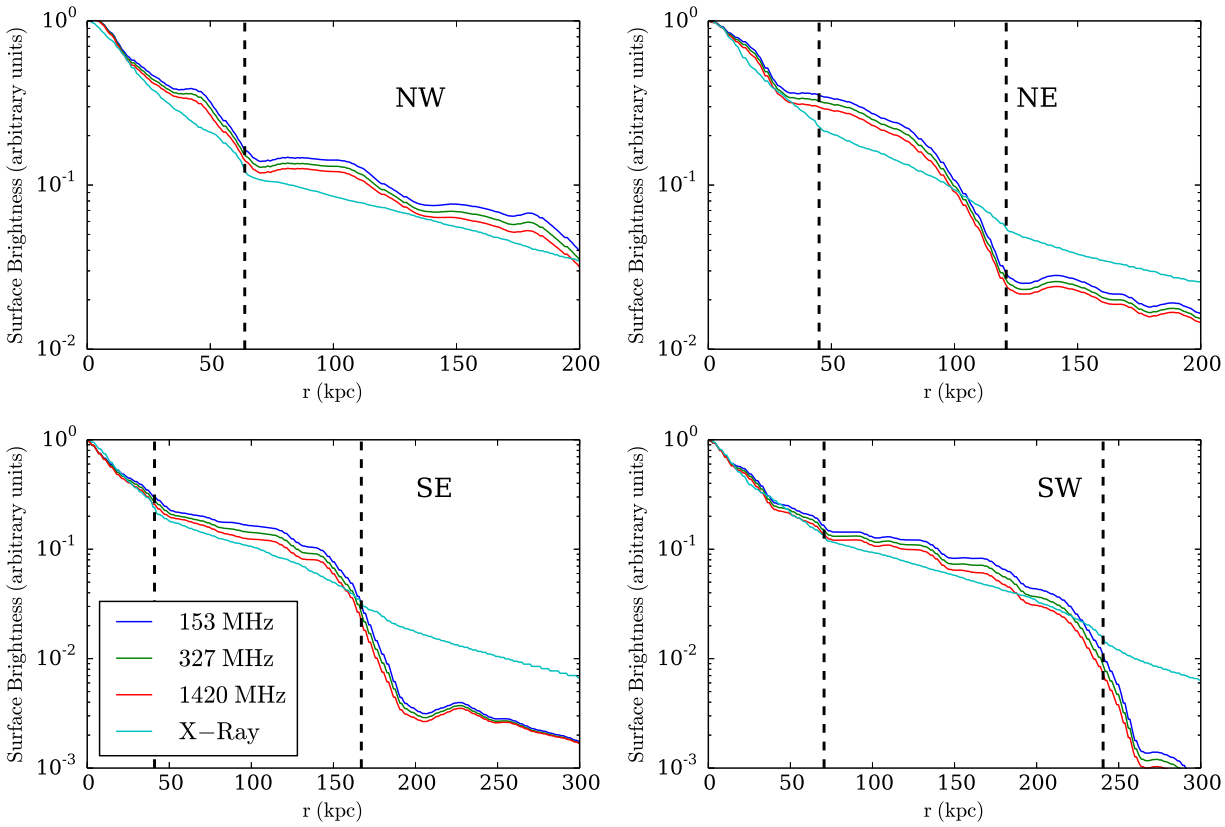

FIG. 6.— Profiles of the X-ray and radio emission (at three different frequencies) at the epoch $t = 3.5$ Gyr (see Figure 5 for profile locations). The emission has been renormalized so that all profiles are unity at $r = 0$ for comparison purposes. The positions of the X-ray cold fronts are marked with black dashed lines.

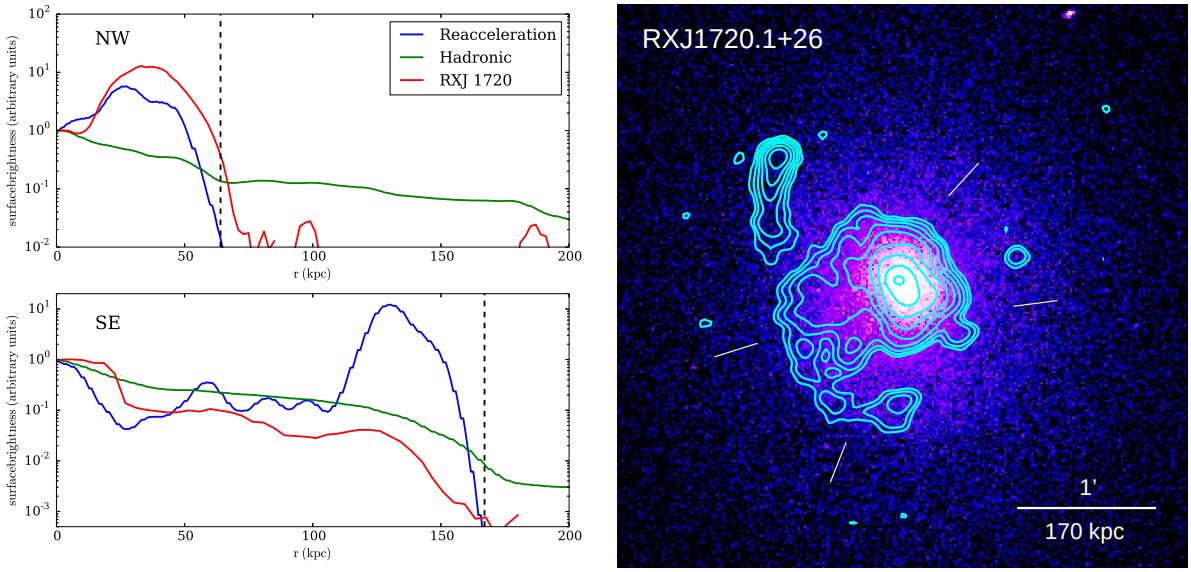

FIG. 7.— Comparisons of radial profiles of radio emission between different models of minihalos and an observation. Left: Profiles of radio emission from the hadronic simulations from this work, the reacceleration simulations from Z13, and from observations of RXJ 1720.1+26 (Giacintucci et al. 2014b), along the northwest and southeast directions. The emission has been renormalized so that all profiles are unity at $r = 0$ for comparison purposes. The profiles from RXJ 1720.1+26 have been rescaled such that the radius of the cold front is the same as that in the simulations. The black dashed lines mark the positions of the cold fronts. Right: X-ray counts image of RXJ 1720.1+26 with 617 MHz radio contours overlaid. Radial white lines mark the two sectors (NW and SE) where the profiles have been generated. The peak in the reacceleration profile at $r \sim 130$ kpc is due to a patch of strong turbulence in this region.

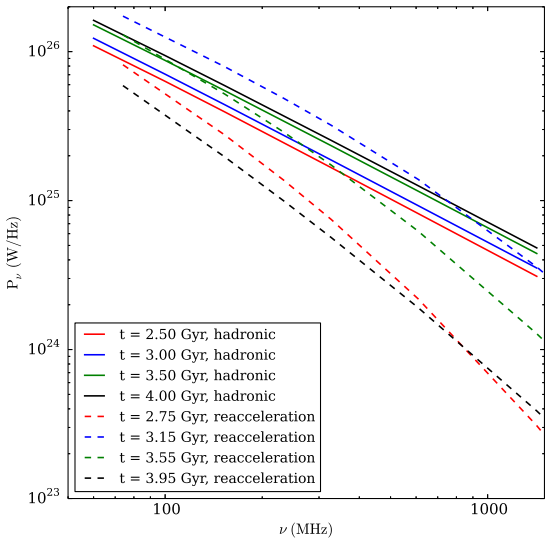

FIG. 8.— The total radio spectrum within a radius of 300 kpc from the cluster center for the hadronic model from this work and the reacceleration model from Z13 at several epochs.

front surfaces where the enhanced magnetic pressure due to shear amplification may become significant).

The main contribution to the drop in radio emission will arise from the difference in the magnetic field across the front (Keshet & Loeb 2010). Below the front, the field will be amplified to $B > B_{\rm CMB}$, and the radio emission is roughly independent of the magnetic field strength. When the fronts reach a large radius, above the front the unamplified field will likely be weak due to the decline of magnetic field strength with radius, with $B < B_{\rm CMB}$, and the radio emission will drop off rapidly as the square of the field. Figure 11 shows the mass-weighted projected magnetic field at the epoch $t = 3.5$ Gyr scaled by $B_{\rm CMB}$. The magnetic field has been amplified to $B > B_{\rm CMB}$ throughout the sloshing region, and for the most part, just outside of the cold fronts the field drops to $B < B_{\rm CMB}$. However, the region to the northwest is filled with strong magnetic field outside of the cold fronts, due to strong velocity shears in that region. Along projected radii in that direction, there will be no drop in emission as one crosses the cold front surface. Clearly, in the hadronic model the radial extent of the minihalo emission depends critically on the magnetic field structure.

This, of course, depends to a certain extent on our initial choice for the magnetic field strength. In our simulation, the magnetic field was initialized such that $\beta = p_B/p_{\rm th} = 100$ (ZML11), and for the simulation used in Z13 and in this work we allowed this configuration to relax. The resulting magnetic field profile from this relaxation peaks at roughly $B \sim 12$ μG at the cluster center, decreases to $\sim$5 μG at the cooling radius, and drops below $B_{\rm CMB}$ at $r \sim 100$ kpc (Figure 1 of ZML11). In some clusters, the magnetic field strength may be even higher than this in the core region due to turbulent-driven amplification caused by AGN, minor mergers, and accretion. More simulations with different magnetic field configurations would be needed in order to determine the conditions under which minihalos would have steep drops in emission at cold front surfaces in the hadronic model.

4.2. *Total Spectrum and Spectral Steepening Along the Cold Fronts*

According to Keshet (2010), rapid magnetic field amplification can cause significant departures from steady-state conditions, which produces synchrotron spectral steepening under the hypothesis of a secondary origin of the emitting particles. If strong, these effects may have important consequences for the origin of minihalos and giant halos. In our simulations we do not see significant effects of this nature. We find that the total spectrum of the minihalo is fairly consistent with a simple power-law in agreement with the expectation based on steady-state conditions. Though we do see some steepening of the synchrotron spectrum near the cold front surfaces that we can confirm is indeed due to magnetic field amplification in these regions, we find that the effect is barely observable, even at very low observing frequencies where it should be maximized. Section 4.3.3 of Keshet (2010) determines the change in spectral index α for a sudden increase in the cooling rate over the injection rate, parameterized by

$$\mathcal{R} = \frac{\psi_f/\mathcal{Q}_f}{\psi_i/\mathcal{Q}_i} = \frac{B_f^2 + B_{\rm CMB,f}^2}{B_i^2 + B_{\rm CMB,i}^2}\frac{n_{\rm th,i}C_{\rm p,i}}{n_{\rm th,f}C_{\rm p,f}}. \quad (12)$$

From Figure 16 of Keshet (2010), we may determine the approximate increase in the magnetic field strength associated with a given spectral steepening. It is instructive to examine the necessary increase in the cooling rate to produce the steepest spectra of any of the particles in the simulation ($\alpha \sim 2$) and the steepest spectra we measure in our spectral index maps ($\alpha \sim 1.3$). For our injection index of $\alpha_p \approx 2$, a sudden increase of $\mathcal{R} \sim 15$ is required to steepen the synchrotron spectrum to $\alpha \sim 2$, whereas for steepening to $\alpha \sim 1.3$ a more modest increase of $\mathcal{R} \sim 3$ is required.

What qualifies as a "sudden" increase? Formally, since in steady-state conditions the characteristic timescale is (Keshet & Loeb 2010):

$$t_{\rm cool} \simeq 0.13 \left[\frac{4\left(\frac{B\sqrt{3}}{B_{\rm CMB,0}}\right)^{-3/2}}{1+\left(\frac{B}{B_{\rm CMB,0}}\right)^{-2}}\right] \nu_{1.4}^{-\frac{1}{2}}(1+z)^{-\frac{7}{2}} \text{ Gyr}, \quad (13)$$

any sudden increase in the cooling rate must occur on a timescale shorter than this in order to significantly affect the spectrum. For $B \lesssim B_{\rm CMB}$, $t_{\rm cool} \sim 0.1 - 0.2$ Gyr for electrons emitting at frequencies between 327 and 1400 MHz.

Motivated by this, we examine the trajectories of a few tracer particles with extreme ($\alpha \sim 2$) spectral indices, to see if these conditions prevail. Figure 12 shows the evolution in $\mathcal{R}$ for three tracer particles with spectral indices $\alpha \sim 2$. $\mathcal{R}$ for each particle is normalized to unity at time t_i, and all times are given with respect to the epoch t_f at which the spectral index is measured, marked by the black dashed line. Each of these particles indeed experiences a sudden increase in $\mathcal{R}$, followed by a rapid decrease. The dot-dashed lines in the figure indicate the necessary $\mathcal{R}$ to steepen the spectrum to the given spectral index from a steady-state, estimated from Figure 16 in Keshet (2010). All of the curves show an increase in $\mathcal{R}$ that is at least this much, and this occurs over roughly

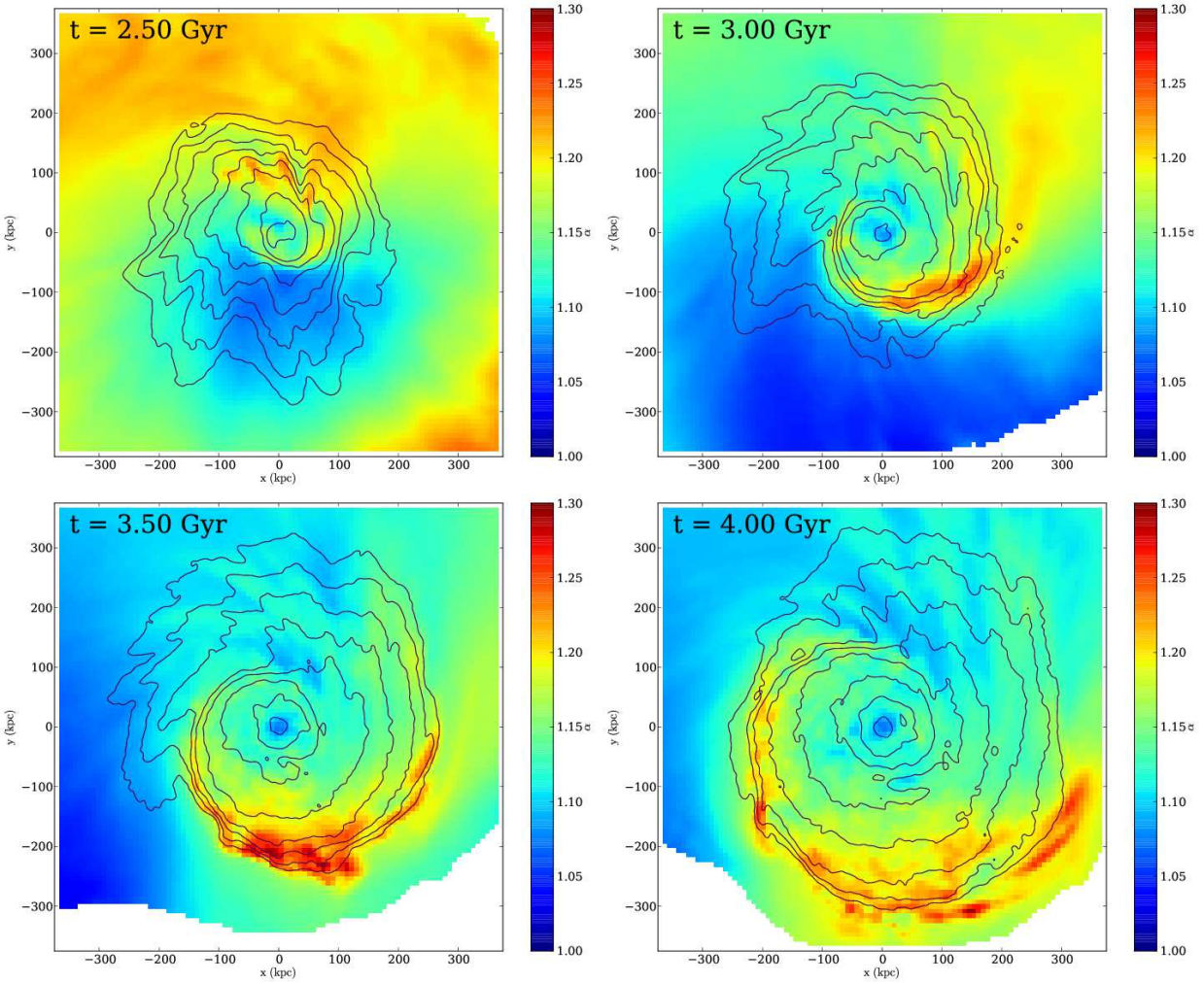

FIG. 9.— Spectral index map at several epochs (between the frequencies of 327 and 1420 MHz) with 327 MHz radio contours overlaid (contours are taken from Figure 5). Each panel is 750 kpc on a side.

a cooling time ($t \sim 0.13$ Gyr), with the most significant increase occurring over a small fraction of that time.

The fact that we find so few tracer particles with very steep spectra indicates that these conditions (required to produce such steepening) do not prevail throughout most of the cluster core. Though there is significant magnetic field amplification (see Figure 11), it does not usually occur fast enough to steepen the spectrum significantly.

4.3. *Limitations of this Work*

The main limitation of this work is that we have not self-consistently solved for the evolution of the CRp population. Instead, we have assumed that the CRp energy density is proportional to the thermal energy density.

Due to this fact, we are not able to model the transport and diffusion of CRp and its connection with the gas dynamics in the sloshing region. Turbulence might transport CRp on a scale that could be of the order of the cluster core, potentially inducing a spatial distribution of CRp that is broader than that of the thermal plasma. Future studies based on passive tracers will allow to follow the transport of CRp and to include this process in our simulations.

Momentum-diffusion of CRs that is mediated by the scattering of particles with MHD waves in the plasma is a different process that is more difficult to model due to the uncertainties in the physics of (small-scale) turbulence in these environments. Plasma instabilities (including the streaming instability) in a weakly-collisional plasma such as the ICM, are expected to increase the scattering rate of CRs resulting in a strong suppression of diffusion along the field lines and typically limiting the drift velocity to the value of the local Alfvén speed. Under these conditions, diffusion is not expected to affect our main conclusions. However, Enßlin et al. (2011) and Wiener et al. (2013) discussed the impact of hypothetical super-Alfvénic CR streaming on the properties of the radio emission generated on cluster scales. In particular, Wiener et al. (2013) calculated the suppression of the streaming instability in a turbulent flow showing that under these conditions the self-generated waves do not limit the particle drift velocity to the Alfvén speed. However, this does not automatically imply that streaming is efficient, because the background turbulence (necessary to suppress the instability) still provides a source of scattering that may make the transport of CRs diffusive and potentially inefficient (see Brunetti & Jones 2014, for a discussion).

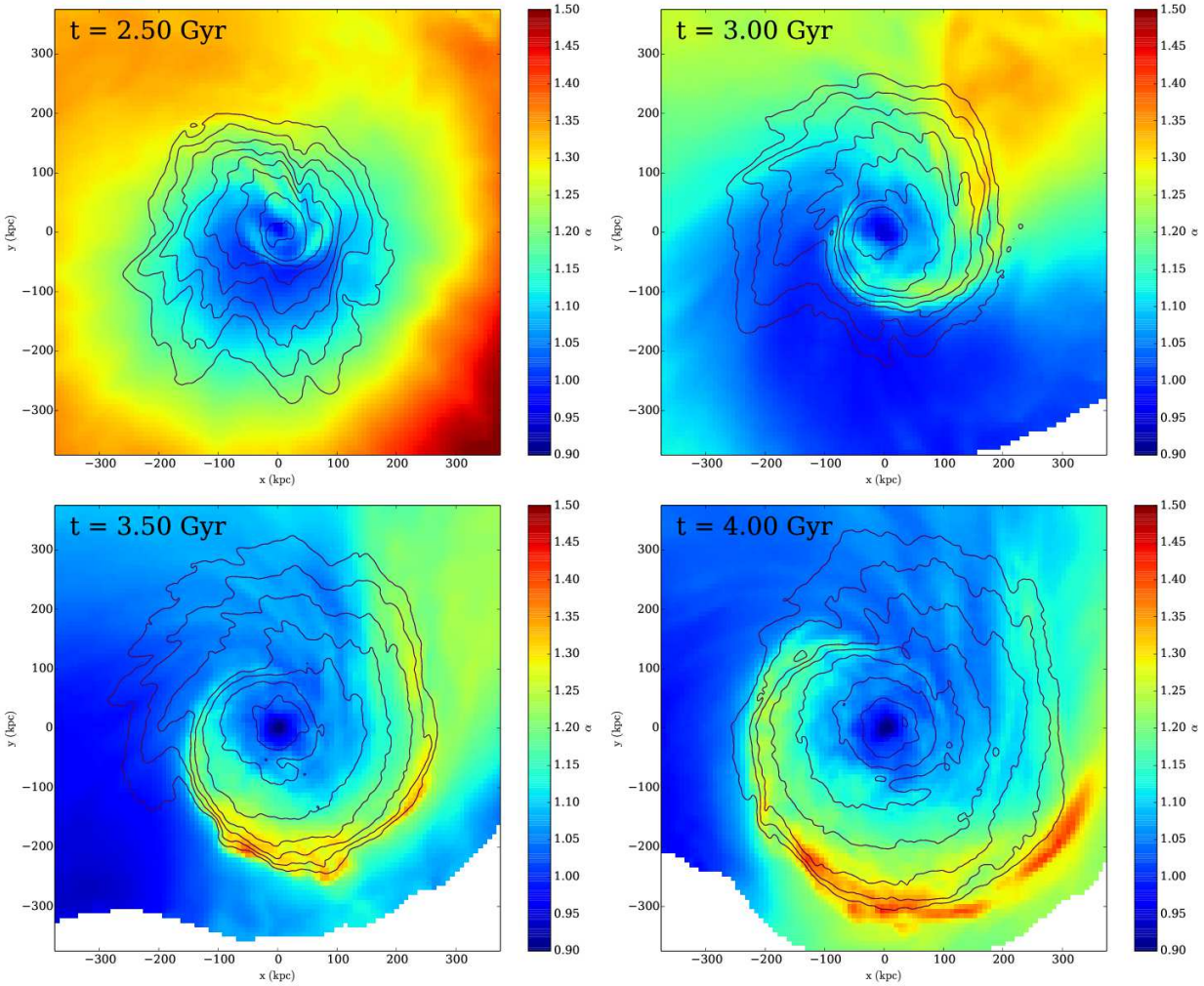

FIG. 10.— Spectral index map at several epochs (between the frequencies of 60 and 153 MHz) with 327 MHz radio contours overlaid (contours are taken from Figure 5). Each panel is 750 kpc on a side.

Also, we assumed a population of CRp with a single power-law spectrum. This implies an injection spectrum of CRe that is power-law in form, and that any steepening of the radio spectrum at higher frequencies comes from strong departures from the steady-state condition. Instead, steepening of the CRe spectrum may reflect possible steepening of the CRp spectrum. Wiener et al. (2013) discussed the possibility of a steepening of the CRp spectral distribution resulting from an efficient momentum-dependent diffusion. This is also not included in our simulations. However, this process would eventually result in a spectral flattening of the synchrotron emission with distance, because higher energy CRp diffuse faster (this effect is unavoidable in the case that we measure variations of the radio spectrum with distance). The observational consequence would be that minihalos would be typically broader if observed at higher frequencies. This differs from expectations based on other models, allowing to discriminate between different origin scenarios for the CRe. For example, reacceleration models eventually predict a spectral steepening with radius or more complex spectral variations (e.g. Brunetti & Jones 2014, and references therein). Another limitation is that we do not include the effect of turbulent reacceleration on the spectrum of both CRp and CRe, a process that is believed to be important, for example, in the case of giant radio halos.

5. SUMMARY

In this work, we have employed a MHD simulation of gas sloshing in a galaxy cluster core to model the formation of a radio minihalo from hadronically originating cosmic-ray electrons. This simulation was previously used to model the formation of a radio minihalo from reaccelerated cosmic-ray electrons by turbulence. We used passive tracer particles to follow the evolution of CRe spectra under the assumption that these electrons are continuously injected by hadronic processes and they undergo radiative (synchrotron and inverse-Compton) and Coulomb losses via interaction with the thermal gas and magnetic fields.

We find that, in this model, the radio emission associated with the minihalo is not completely confined within the core region. Along some radial directions that cross cold front surfaces, the radio emission drops steeply at these surfaces, due to the magnetic field amplification below the cold fronts but not above them. However, along other directions, the magnetic field strength changes less

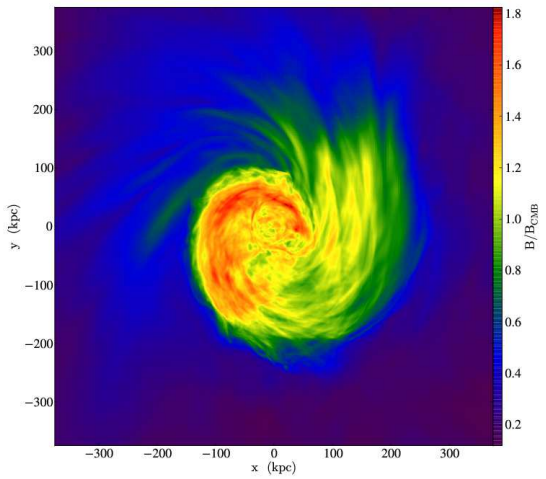

FIG. 11.— Mass-weighted projection of the magnetic field strength scaled by $B_{\rm CMB}$. The panel is 750 kpc on a side.

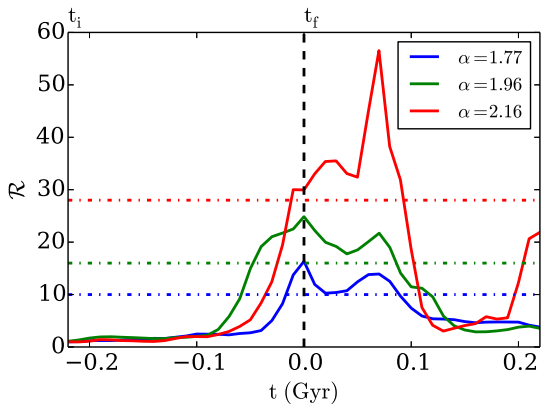

FIG. 12.— Evolution of the ratio of the cooling rate to the injection rate $\mathcal{R}$ for three different tracer particles with extreme spectral indices. Times are rescaled to t_f (for each particle), the epoch at which the spectral index is measured, marked by the black dashed line. The ratio $\mathcal{R}$ is rescaled so that its value is unity at t_i. The colored dot-dashed lines indicate the value of $\mathcal{R}$ for the corresponding particle required to steepen its spectrum to its spectral index value at t_f, estimated from Figure 16 of Keshet (2010).

sharply at the fronts and as a result the radio emission decreases much more smoothly with radius, in concert with the mild decline in X-ray emission. Based on our numerical studies from this work and Z13, we believe that the relationship between X-ray and synchrotron brightness in these sources is a viable tool to discriminate between different origin models of the emitting CRe. For example, our expectations based on our hadronic model are in tension with observations of a few of the best-observed minihalos, which show the radio emission confined to roughly the size of the core region in all directions (Mazzotta & Giacintucci 2008; Giacintucci et al. 2011, 2014a). However, the few observations currently available do not permit us to make firm conclusions.

Our simulations allow us to go beyond the steady-state approach commonly adopted in secondary models. We find that some steepening of the synchrotron spectrum does occur in minihalos due to rapid magnetic field amplification caused by sloshing. For some test particles, this effect is significant, with radio spectra as steep as $\alpha \approx 2$ (compared to the steady-state, and prevalent, value of $\alpha = 1.13$). However, the emission from these particles makes up a very small fraction of the total emission from the CRe. As a result, we find that the total spectrum of the minihalo is a power law, consistent with that expected from assuming steady-state conditions. Effects of rapid magnetic field amplification start to be visible when we consider synchrotron spectral index maps. In these, we see some steepening in the region of the cold fronts where magnetic field amplification is stronger. However these effects induce only marginal variations of $\Delta\alpha \sim 0.1$-0.15 between 327-1420 MHz and $\Delta\alpha \sim 0.2$-0.25 between 60-153 MHz as one goes outward along the cold fronts, where magnetic field amplification is strongest. This differs from our previous results based on the same underlying numerical simulation under the hypothesis that the emitting electrons are reacccelerated by turbulence, where the spectral index is predicted to steepen more than this at high frequencies. Consequently, we conclude that spectral studies of radio mini-halos (such as in Murgia et al. 2010; Giacintucci et al. 2014b) are important as they allow discriminations between these different models.

Future work will need to incorporate the dynamics of the CRp self-consistently to determine to what extent it plays a role in shaping the radio emission from minihalos. Additionally, a fuller picture of the cause of such emission may arise from the combination of the effects of hadronic injection of CRe and their subsequent turbulent reacceleration, a merger of the two currently competing models, which has already been investigated for giant radio halos from a theoretical perspective (Brunetti & Blasi 2005; Brunetti & Lazarian 2011).

JAZ thanks Uri Keshet for useful discussions. Analysis of the simulation data was carried out using the AMR analysis and visualization toolset yt (Turk et al. 2011), which is available for download at `http://yt-project.org`. JAZ is supported under the NASA Postdoctoral Program. GB acknowledges partial support by grant PRIN-INAF-2009. The software used in this work was in part developed by the DOE-supported ASC / Alliances Center for Astrophysical Thermonuclear Flashes at the University of Chicago.

REFERENCES

Ackermann, M., Ajello, M., Allafort, A., et al. 2010, ApJ, 717, L71
Ascasibar, Y., & Markevitch, M. 2006, ApJ, 650, 102
Blasi, P., & Colafrancesco, S. 1999, Astroparticle Physics, 12, 169
Bonafede, A., Feretti, L., Murgia, M., et al. 2010, A&A, 513, A30
Brunetti, G., Setti, G., Feretti, L., & Giovannini, G. 2001, MNRAS, 320, 365
Brunetti, G. 2003, Matter and Energy in Clusters of Galaxies, 301, 349
Brunetti, G., & Blasi, P. 2005, MNRAS, 363, 1173
Brunetti, G., & Lazarian, A. 2007, MNRAS, 378, 245

Brunetti, G., & Lazarian, A. 2011, MNRAS, 410, 127
Brunetti, G., & Jones, T. W. 2014, arXiv:1401.7519
Burns, J. O., Sulkanen, M. E., Gisler, G. R., & Perley, R. A. 1992, ApJ, 388, L49
Cassano, R., Gitti, M., & Brunetti, G. 2008, A&A, 486, L31
Dolag, K., & Enßlin, T. A. 2000, A&A, 362, 151
Dubey, A., Antypas, K., Ganapathy, M. K., Reid, L. B., Riley, K. M., Sheeler, D., Siegel, A., Weide, K. Extensible component based architecture for FLASH, a massively parallel, multiphysics simulation code. Parallel Computing 35 (10-11), 512–522.
Enßlin, T., Pfrommer, C., Miniati, F., & Subramanian, K. 2011, A&A, 527, A99
The *Fermi*-LAT Collaboration: Ackermann, M., et al. 2013, arXiv:1308.5654
Fujita, Y., & Ohira, Y. 2012, ApJ, 746, 53
Ghizzardi, S., Rossetti, M., & Molendi, S. 2010, A&A, 516, A32
Giacintucci, S., Markevitch, M., Brunetti, G., Cassano, R., & Venturi, T. 2011, A&A, 525, L10
Giacintucci, S., Markevitch, M., Venturi, T., et al. 2014, ApJ, 781, 9
Giacintucci, S., et al. 2014, in preparation.
Gitti, M., Brunetti, G., & Setti, G. 2002, A&A, 386, 456
Gitti, M., Ferrari, C., Domainko, W., Feretti, L., & Schindler, S. 2007, A&A, 470, L25
Gitti, M. 2013, MNRAS, 436, L84
Govoni, F., Murgia, M., Markevitch, M., et al. 2009, A&A, 499, 371
Hlavacek-Larrondo, J., Allen, S. W., Taylor, G. B., et al. 2013, ApJ, 777, 163
Kelner, S. R., Aharonian, F. A., & Bugayov, V. V. 2006, Phys. Rev. D, 74, 034018
Keshet, U., & Loeb, A. 2010, ApJ, 722, 737
Keshet, U. 2010, arXiv:1011.0729
MAGIC Collaboration, Aleksić, J., Alvarez, E. A., et al. 2011, arXiv:1111.5544
Markevitch, M., & Vikhlinin, A. 2007, Phys. Rep., 443, 1
Mazzotta, P., & Giacintucci, S. 2008, ApJ, 675, L9
Murgia, M., Eckert, D., Govoni, F., et al. 2010, A&A, 514, A76
Pfrommer, C., & Enßlin, T. A. 2004, A&A, 413, 17
Pfrommer, C., Enßlin, T. A., & Springel, V. 2008, MNRAS, 385, 1211
Prokhorov, D. A., & Churazov, E. M. 2013, arXiv:1309.0197
Roediger, E., Brüggen, M., Simionescu, A., Böringer, H., Churazov, E., & Forman, W. R. 2011, MNRAS, 369
Roediger, E., & ZuHone, J. A. 2011, arXiv:1109.2593
Rybicki, G. B., & Lightman, A. P. 1979, New York, Wiley-Interscience, 1979. 393 p.
Sarazin, C. L. 1999, ApJ, 520, 529
Sijbring, D. 1993, Ph.D. Thesis, Groningen
Smith, R. K., Brickhouse, N. S., Liedahl, D. A., & Raymond, J. C. 2001, ApJ, 556, L91
Turk, M. J., Smith, B. D., Oishi, J. S., Skory, S., Skillman, S. W., Abel, T., & Norman, M. L. 2011, ApJS, 192, 9
Vazza, F., Roediger, E., & Brüggen, M. 2012, A&A, 544, A103
Wiener, J., Oh, S., & Guo, F. 2013, arXiv:1303.4746
Zandanel, F., Pfrommer, C., & Prada, F. 2014, MNRAS, 438, 124
ZuHone, J. A., Markevitch, M., & Johnson, R. E. 2010, ApJ, 717, 908 (ZMJ10)
ZuHone, J. A., Markevitch, M., & Lee, D. 2011, ApJ, 743, 16 (ZML11)
ZuHone, J. A., Markevitch, M., Brunetti, G., & Giacintucci, S. 2013, ApJ, 762, 78 (Z13)